The Low Frequency Edge Oscillation in Alcator C-Mod and ASDEX Upgrade I-Mode

W. McCarthy[1*], A. E. Hubbard[2], J. Terry[2], B. Labombard[2], A. Kuang[3], R. Bielajew[2], I. Hutchinson[2], J. W. Hughes[2], D. Silvagni[4], T. Happel[4], L. Gil[5], The Alcator C-Mod Team[2], The ASDEX Upgrade Team[4]

1 – Worcester Polytechnic Institute, Department of Physics
2 – Massachusetts Institute of Technology, Plasma Science and Fusion Center
3 – Commonwealth Fusion Systems
4 – Max-Planck-Institut für Plasmaphysik, Boltzmannstr. 2, 85748 Garching, Germany
5 – Instituto de Plasmas e Fusão Nuclear, Instituto Superior Técnico, Universidade de Lisboa
* - Corresponding Author: wcmccarthy@wpi.edu

Abstract

The Low Frequency Edge Oscillation (LFEO) is a low frequency fluctuation in many plasma quantities in the pedestal region of the I-Mode confinement regime. It is observed on Alcator C-Mod between 10-30kHz and on ASDEX Upgrade between 5-10kHz. On both tokamaks it has been previously identified as a Geodesic Acoustic Mode (GAM), however the recent discovery of the Edge Temperature Ring Oscillation (ETRO) in a similar frequency and spatial location as the LFEO in I-Modes on EAST has called this identification into question. In this paper we investigate the LFEO on C-Mod and AUG using a variety of different experimental techniques including spectral analysis, magnetic mode number analysis, localization, and direct measurement of the LFEO zonal structure and propagation using a Mirror Langmuir Probe. This investigation has reconfirmed the identification of the LFEO as a GAM and determined that it has several key differences from the ETRO.

1. Introduction

It is desirable for a future nuclear fusion reactor to operate in a regime that demonstrates high energy confinement. The most common of these confinement regimes is the High Confinement Mode (H-Mode) [1], which demonstrates strong particle and energy confinement with pedestals in density and temperature forming in the edge. However, most H-Modes suffer from high impurity confinement, which can cause increased radiation, and edge localized modes which can pose a threat to material surfaces. An alternative to the H-Mode is the Improved Confinement Mode (I-Mode) [2,3].

The I-Mode confinement regime was first discovered on the ASDEX-Upgrade tokamak (AUG) and the Alcator C-Mod tokamak as a transient mode [4–6] and later as a stationary mode [2,7]. It has since also been observed on the the DIII-D [8],EAST [9] and KSTAR tokamaks. It is a confinement mode that is characterized by an H-Mode-like temperature pedestal, an Low Confinement Mode (L-Mode) like density profile, L-Mode-like impurity confinement, and a reduction relative to L-mode in broadband density fluctuation intensity. The I-Mode has been shown to be intrinsically stable against edge localized modes [10,11], however it does exhibit smaller Edge Localized Mode (ELM) like pedestal relaxation events (PREs) as it approaches H-Mode [12,13]. I-Mode is almost universally accessed in the "unfavorable" grad-B configuration where the grad-B drift is pointed away from the active x-point. The

L-I transition can develop quickly, similar to the L-H transition, however it can also develop over a slower time scale [2].

A common feature of I-Mode is the development of a high frequency Weakly Coherent Mode (WCM), around ~300 kHz on Alcator C-Mod, around ~90kHz on AUG with a reduction of fluctuation intensity below that frequency in the pedestal. The WCM has been observed on most devices that have achieved steady I-Mode [2,4,9,14]. An exception is DIII-D which has accessed a regime with similar conditions and temperature pedestals, but where WCM has not been observed to date [8]

A second, Low Frequency Edge Oscillation (LFEO) [15], is also often, observed in I-Mode at C-Mod and AUG. An example of a WCM and a LFEO on C-Mod can be seen in Figure 1. On both machines, the LFEO has previously been identified as a Geodesic Acoustic Mode (GAM) [4,16]. It should be noted that while the LFEO is very common in I-Mode, it is not ubiquitous in I-Mode and I-Modes have been observed that did not have a detectable LFEO.

On EAST, [17,18] a similar low frequency oscillation has been identified as an Edge Temperature Ring Oscillation (ETRO). While it is possible that LFEO/GAM observed on C-Mod and AUG is a fundamentally different mode than the ETRO observed on EAST, the fact that all three live in the edge, in a similar frequency range, and exhibit nonlinear coupling with the WCM, suggests that they are somehow linked.

These coherent low frequency (5kHz-40kHz) fluctuations (LFEO/ETRO/GAM) may play an important role in I-Mode physics, therefore it is important to study them. For instance, quasicoherent fluctuations are thought to be responsible for the stationarity of the Enhanced D-Alpha (EDA) H-Mode on C-Mod [19,20] and AUG [21]and the Quiescent H-Mode on DIII-D [22,23] and AUG [24]. Additionally, it has been shown that the GAM can have a role in the regulation of turbulent transport via the shear flows it generates [25]. Specifically, it has been shown on both C-Mod [16,26] and AUG [4] that the GAM has non linear coupling to the WCM and may be responsible for the “weak” nature of the WCM.

A natural question to ask is, are the LFEO and ETRO, in fact, the same mode and one has been misidentified? With that in mind, for clarity, we will refer to the experimentally observed low frequency fluctuation on C-Mod and AUG as the LFEO and compare it to both the theoretical predictions of the GAM and the reported experimentally observed features of the ETRO.

In this paper, we investigate the spatial and spectral characteristics of the LFEO on C-Mod and AUG, with a particular focus on its identification. In Section 2, we briefly discuss C-Mod and AUG and the relevant diagnostics used in this study. In Section 3, we summarize the physics behind the GAM and highlight some of the reported features of the ETRO. In Section 4, we discuss the general characteristics of the LFEO on C-Mod and AUG. In Section 5, we directly measure the radial structure of the LFEO using a combination of a Scanning Langmuir Probe and a Gas Puff Imaging system on C-Mod. In Section 6 we compare the LFEO, GAM, and ETRO and draw conclusions about the identity of the LFEO. Finally, in Section 7, we provide a summary.

In doing so we will reconfirm the identification of the LFEO on C-Mod and likely on AUG as a GAM and demonstrate several key differences between the LFEO and ETRO seen on EAST.

2. Diagnostic Setup

In this paper we investigate the LFEO in two tokamaks: Alcator C-Mod, [20,27,28] which was operated by the Massachusetts Institute of Technology until 2016, and ASDEX Upgrade [29], which is operated in Germany by the Max Planck Institute for Plasma Physics. Their parameter operation spaces are shown in table 1.

2.1 Profile Measurements

As the LFEO exists primarily within the pedestal, and we are investigating the precise location and frequency structure of the LFEO, accurate measurements of the plasma profiles in the pedestal are important.

For our analysis of C-Mod, electron density and temperature profiles are generated using a Gaussian Process Regression (GPR) [30] fit to data from a Thomson Scattering (TS) system [31]. When possible, the TS data is supplemented with Electron Cyclotron Emission (ECE) data [28] to obtain the electron temperature profile.

On AUG, plasma profile information is provided by Integrated Data Analysis (IDA) [32] which performs forward modeling of plasma temperature and density using a number of different diagnostics including TS [33], Electron Cyclotron Emission [34], a lithium beam diagnostic [35], and an interferometer [36].

2.2 Magnetic Coordinates

On both C-Mod and AUG, radial coordinates from the center of the plasma are based on normalized poloidal flux [15]. On C-Mod normalized poloidal flux is typically used:

$$\psi_n = \frac{\Psi - \Psi_a}{\Psi_{LCFS} - \Psi_a} \tag{1}$$

where Ψ_a and Ψ_{LCFS} are the poloidal fluxes on the magnetic axis and the LCFS respectively. On AUG, it is standard to take the square root of this quantity ($\rho_p = \sqrt{\psi_n}$). For the sake of clarity, results from both machines will be reported using ψ_n in this paper.

On C-Mod, magnetic equilibrium and magnetic flux were calculated using the EFIT reconstruction code [37] and on AUG, they were calculated using the CLISTE code [38].

2.3 Fluctuation Diagnostics

The LFEO is observable in many different plasma parameters and thus we characterize it with a wide array of diagnostics including: Mirnov Coils, Reflectometry, Electron Cyclotron Emission radiometer, Langmuir Probes, and Gas Puff Imaging. The individual systems used in this paper on each machine are outlined below.

C-Mod Magnetic Fluctuations

Mirnov Coil Array [39]: Magnetic fluctuations on C-Mod are used to do magnetic mode number analysis in Section 4.

C-Mod Density Fluctuations

Reflectometry [40]: On C-Mod, the Ordinary mode (O-Mode) reflectometer is used to measure density fluctuations and probes the plasma at a number of fixed frequencies.

Gas Puff Imaging [16]: The Gas Puff Imaging (GPI) system on C-Mod was used by Cziegler et. al. [16] for the original identification of the LFEO as a GAM in I-Mode. The emissivity of an injected neutral gas is measured using a 9 X 10 array of viewing cords (3.8mm spot size, 3.9mm spatial resolution). Fluctuations in emissivity typically are treated as density fluctuations since the emissivity dependence on temperature is weak.

Divertor Langmuir Probes [41]: On C-Mod, the LFEO has been observed in fluctuations in the ion saturation current of divertor Langmuir probes.

AUG Density Fluctuations

Conventional Reflectometry [42]: the conventional frequency hopping reflectometry system (O-Mode) on AUG uses a single, but variable (33-49 GHz) frequency to probe the plasma.

C-Mod Temperature Fluctuations

FRC-ECE [28,43]: The Fusion Research Center ECE (FRC-ECE) is a conventional fast heterodyne ECE system that measures electron temperature on C-Mod. It has 32 channels with fixed measurement frequency. The poloidal and radial resolution are set by mapping of the off-midplane view to the midplane.

AUG Temperature Fluctuations

Conventional ECE [44,45]: The conventional ECE system on AUG has 60 frequency channels spanning nearly the entire confined region and into the outer Scrape off Layer (SOL). In the edge it has a spatial resolution of $\sim .5cm$.

CECE [46]: The Correlation Electron Cyclotron Emission (CECE) diagnostic on AUG was designed to measure temperature fluctuations in the pedestal. It has a radial resolution of roughly $2-4mm$ in between channel centers. In Section 4 we use it to precisely localize the LFEO in the pedestal.

C-Mod Hybrid Fluctuation Diagnostics

Scanning MLP [19]: The scanning Mach Mirror Langmuir Probe (MLP) on C-Mod [19] is made up of 4 probe tips arranged in a pyramidal Mach probe configuration. It is inserted into the plasma above the outer midplane up to and just past the LCFS. An advanced biasing scheme allows it to sample n_e, T_e, and ϕ_p (plasma potential) fluctuations at $1.1MHz$ time resolution. It is common to report the position of the probe with coordinate ρ which indicates the distance outside of the LCFS location (a negative number means the probe is inside the LCFS) determined by EFIT when mapped to the outer midplane.

3. The Geodesic Acoustic Mode and the ETRO

3.1 GAM

The GAM has been discussed extensively in literature for both theory [47–52] and experiment [53–58] and its relation to zonal flows has been well established [59]. An excellent review paper on the subject has been written by Conway [60], but we summarize the basic concepts relevant for this work here.

In a circular cross section geometry, the GAM is a toroidally and poloidally symmetric (n=0, m=0) radial electric field perturbation that results in a poloidal plasma flow through the EXB velocity, which peaks at the outer midplane and has a minimum at the inner midplane. The toroidal geometry of the magnetic field causes this flow perturbation to couple to a poloidally anti symmetric (n=0, m=1) pressure perturbation that is considered to generally be dominated by the density perturbation. The poloidal gradient in density results in a diamagnetic current across flux surfaces. This diamagnetic current balances with the polarization current caused by the fluctuating electric field such that only an (n=0,m=2) cross field return current survives, which acts both to reverse the potential structure (making the GAM oscillate) and to generate an (n=0,m=2) magnetic perturbation [61]. The structure of the GAM is shown in cartoon form in Figure 2.

The frequency of the GAM oscillation in a circular cross section tokamak derived from cold ion fluid equations is canonically given as:

$$\omega_{G,f} = \frac{c_s}{R} \tag{2}$$

Where $c_s = \sqrt{2T_e/m_i}$, and R is the major radius of the tokamak at the point the GAM frequency is calculated. The full fluid derivation can be found in [15]. More complicated derivations of the GAM that consider shaping [62], plasma rotation [63], and impurity content using gyrokinetic theory [49] have been performed. When calculated from gyrokinetic theory, which includes elongation and different ion and electron temperatures, the GAM frequency is given by:

$$\omega_{G,gyro} = \sqrt{\frac{2}{\kappa^2+1}}\frac{\sqrt{7+4\tau_e}v_{ti}}{2R}\left(1+\frac{(23+16\tau_e+4\tau_e^2)(\kappa^2+1)}{(7+4\tau_e)^2q^2}\right) \tag{3}$$

Where $\tau_e = T_e/T_i$, κ is the elongation, and $v_{ti} = \sqrt{2T_i/m_i}$ is the ion thermal velocity. The density and potential fluctuations are related in a circular cross section by [59]:

$$\frac{\tilde{n}_{GAM}}{n_0} = -\left(\sqrt{2}k_r\rho_i\frac{e\tilde{\phi}}{T_e}\right)\sin\theta \tag{4}$$

Where k_r, ρ_i are the radial wave number of the GAM and the ion Larmor radius respectively, $\tilde{\phi}$ is the potential fluctuation amplitude and θ is the poloidal angle from the outer midplane. It should be noted that the spatial distribution can be significantly impacted by higher order effects [51], non-circular shaping [62] of the plasma, and rotation in the plasma [47]. Thus, it is possible that, due to higher order harmonics, the null in the density fluctuation will occur at an angle other then $\theta = 0$ [51,60]. However, Equation 4 still provides a good first order estimate of the relative fluctuation amplitudes of potential and density to compare to data.

It has been shown in more complicated derivations of GAM structure, that the GAM can either take on a standing wave-like structure or a propagating wave-like structure [51]. In the former case, $\tilde{n}_{GAM}$ and $\tilde{\phi}_{GAM}$ are radially 90^o out of phase, whereas in the latter case, $\tilde{n}_{GAM}$ and $\tilde{\phi}_{GAM}$ are radially in phase. $\tilde{n}_{GAM}$ sign relative to $\tilde{\phi}_{GAM}$ is set by the direction of GAM propagation, with it being positive above the midplane for an inward propagation [51]. No agreed upon theory predicts the radial direction of GAM propagation. However, some work has been done on the topic [52] and it is generally believed that it propagates away from the location of GAM drive [60].

Simulations of the GAM on the TCV [64] tokamak have shown that it can take on either a continuum form, where the frequency varies radially with local temperature, or an eigenmode form, where the frequency is radially constant and independent of local temperature and only changes in steps. This eigenmode-like behavior has been observed experimentally in a variety of tokamaks [53,56,64]. Additionally, avalanche-like modes near the GAM frequency have been observed at TCV [65].

3.2 ETRO

The ETRO has been experimentally observed in EAST I-Mode plasmas and reported on in a series of excellent studies by Feng et. al. [9] and Liu et. al. [17,18] which are briefly summarized in this section. It is seen in nearly all stationary I-Modes on EAST, observed in a wide array of diagnostics, and is comprised primarily of a toroidally and poloidally symmetric (n=0, m=0) temperature fluctuation. The ETRO is seen to have a fluctuation in density; however, the temperature fluctuation has a larger maximum amplitude with $\tilde{T}_e/T_e \sim .09$ and $\tilde{n}_e/n_e < .02$. It is also observed by magnetic probes and on divertor Langmuir probes. The ETRO magnetic structure has been shown to be toroidally symmetric and poloidally asymmetric ($n = 0, m = 1$). The ETRO reaches its maximum amplitude near the pedestal top at normalized toroidal flux values $\rho_t < 0.9$, but vanishes in regions closer to the LCFS. Based on these characteristics and the ETRO frequency, Liu et. al. have concluded that the ETRO is not a GAM.

It is believed that the ETRO mediates a rapid transition back and forth between Ion Temperature Gradient (ITG) or Kinetic Ballooning Mode dominated turbulence and Trapped Electron Mode (TEM) dominated turbulence. This determination was made through careful measurements of the turbulent spectra via Doppler reflectometry. The resulting flux is postulated to be the mechanism that allows EAST to operate in steady state I-Mode.

4. General Characteristics of the LFEO

To better understand the LFEO and begin to compare it to the GAM and ETRO, we will describe some of its basic characteristics including: its localization, magnetic mode number, and frequency.

4.1 Localization

We investigate the radial localization of the LFEO on C-Mod using the FRC-ECE and Reflectometry. For shot 1160816011, the autopower spectra for the edge FRC-ECE channels and an edge reflectometry channel are plotted in Figure 3. The LFEO is clearly observed on FRC-ECE channels near and above the top of the pedestal, $\psi_n = 0.964, 0.914$ where it is strong (the pedestal top is $\psi_n \approx .96$), but in the next

channel further in, $\psi_n = 0.86$, it has vanished. It is also seen in the channel just outside the LCFS, $\psi_n = 1.016$. Due to the FRC-ECE line of sight not being perfectly perpendicular to the magnetic field at the edge, the integration width likely penetrates inside the LCFS (i.e. fluctuations occurring at $\psi_n < 1$ may be observed at the $\psi_n = 1.016$). Further, this channel is extremely optically thin so density fluctuations account for a significant portion of the fluctuation intensity and may also be measuring radiation from deeper in the plasma. The edge reflectometry channel measuring at $\psi_n = 0.925$ also clearly observes the LFEO. It should be noted that the large density fluctuation of the LFEO can shift the localization of this channel. As we will see in section 5, the measured density fluctuations are up to $\tilde{n}_{e,exp}/n_0 = 0.1$, which when applied to the whole profile, can shift the reflectometry channel position by up to $\Delta\psi_n \pm .025$.

On AUG the diagnostic allows us to resolve temperature fluctuations throughout the pedestal using CECE [46]. The auto power spectrum for CECE channels with $0.88 < \psi_n < 1$ are shown in Figure 3. In Figure 4, we calculate the fraction of the spectral power contained in the LFEO and WCM frequency bands using $RP = \int_{f_1}^{f_2} AP(f)df \Big/ \left(\int_0^{f_N} AP(f)df - \int_{f_{wcm1}}^{f_{wcm2}} AP(f)df\right)$ where RP is the relative power, AP is the auto power, f_1, f_2 are the lower and upper bound of the LFEO frequency (5.8kHz and 9.8kHz) or WCM frequency (13.5kHz and 120kHz), and f_N is the Nyquist frequency (2MHz). In denominator of both cases, we subtract the power contained in the WCM band. We do this to prevent the relative LFEO energy from being influenced by the presence of the WCM, as the WCM only appears strongly in a single channel. The mode is strongest just below the midpoint of the pedestal and just slightly further up the pedestal than the WCM. The auto power falls off rapidly from its peak in both directions and is barely visible just past the pedestal top which is around $\psi_n = .88$. Note that the WCM is much more localized near the bottom of the pedestal.

Thus, we claim with some confidence, that the LFEO spans from inside the top of the pedestal to near the LCFS in the $0.88 < \psi_n < 1.0$ range, but likely not much deeper toward the core.

We should take special notice of the fact that the LFEO appears at the same frequency throughout its radial extent. This suggests that its drive may be anywhere in this region and does not respond to the changing plasma conditions throughout the pedestal, consistent with an eigenmode like GAM [65]. On both machines, the LFEO appears in the same radial position as the WCM. This is consistent with previous observations of the GAM on C-Mod [16] and with the ETRO on EAST [18]. However, on EAST, both the ETRO and WCM are reported to be localized to the pedestal top and do not extend to the LCFS.

4.2 Magnetic Mode Number

We performed mode number analysis using pairs of Mirnov coils on C-Mod. This was done by taking the cross coherence and cross phase between two coil pairs that are either at fixed poloidal (toroidally separated) or fixed toroidal (poloidally separated) positions. We then chose the cross phase at the highest coherence within the LFEO frequency range. The mode number is calculated as:

$$n, m = -\frac{\Theta}{\delta\alpha_{n,m}} \tag{5}$$

where Θ is the cross phase and $\delta\alpha$ is the angular separation between the coils. The signal from each coil was separated into 366 statistically independent segments and the cross phase was calculated from the ensemble average spectral powers. Error bars were calculated following the procedure in [66] for finding the standard deviation from the cross coherence. For the toroidal mode number analysis shown in Figure 5, 21 pairs of coils at fixed poloidal position with toroidal separations spanning from 5-165 degrees were used. They revealed a toroidal magnetic mode number $n < 1$ not inconsistent with the expectations of $n = 0$ for a GAM or the observed $n = 0$ mode structure of the ETRO. Poloidal mode number analysis was carried out using 20 pairs of coils. The toroidal angle of the coils in each pair was the same, however, the pairs were distributed toroidally around the torus. The poloidal separation of the coils in each pair spanned from 7 to 100 degrees. This analysis is shown in Figure 5 most points fall along the $m = 2$ trend line consistent with the predicted $m = 2$ magnetic fluctuations of the GAM [61] and with previous measurements of the GAM on TCV [67]. However, as is seen in Figure 5, the scatter is large and the coils with the largest angular separation (between $85^o \; and \; 100^o$) show a mode number closer to $m = 1.5$. The magnetic poloidal mode structure of the ETRO has been measured to be $m = 1$.

4.3 LFEO Frequency

A comparison between LFEO and theoretical GAM frequency is shown in Figure 6. The canonical GAM scaling (Equation 2) is modified to include the elongation prefactor in Equation 3 (i.e. $\sqrt{2/(\kappa^2+1)}$), and shown in Figure 6a. It shows decent agreement with the measured LFEO frequencies (with a Pearson Correlation Coefficient of about .4 and a slope of .7), lending strength to the argument that the LFEO is a GAM. The gyrokinetic scaling (Figure 6b), which includes finite ion temperature effects, overpredicts the LFEO frequency. However, the LFEO frequencies still scale roughly with the $\sqrt{T_e}$ dependence of the GAM (with a Pearson Correlation Coefficient of about .4 although with a slope of .5) and are only off by a factor of about two. This is consistent with prior studies of the GAM on C-Mod [16].

We found the best agreement between LFEO and GAM frequencies when we used temperatures from $\psi_n = .98$. This is consistent with our observations that the LFEO is likely driven closer to the bottom of the pedestal (section 4.1). However, using a uniform location for all shots does introduce potential error if the LFEO is not always driven on the same flux surface, which is likely. The calculation of the theoretical GAM frequency is also highly sensitive to the quality of the pedestal profile fit. Small errors in the pedestal fit, in the magnetic reconstruction, or in the underlying temperature measurement can result in large differences in GAM frequency across the pedestal. The LFEO appearing at frequencies lower than those expected for a GAM is consistent with reported observations of the ETRO on EAST.

The points in Figure 6 were obtained by taking time slices of I-Modes between $50 - 200ms$ in length. Electron density and temperature profiles (section 2.1) were shifted such that the electron temperature at $\psi_n = 1$ agreed with the separatrix electron temperature predicted by a 2-point power balance model [68]. Elongation κ and safety factor q were taken from EFIT. $T_e = T_i$ was assumed for the above analysis. LFEO frequency was obtained via Gaussian fits to the LFEO frequency band in the power spectral density from available divertor probes.

4.4 Frequency Chirping

In Figure 7 we show the LFEO frequency responding to the sawtooth heat pulse arriving at the edge. On both AUG (Figure 7a) and C-Mod (Figure 7b) the arrival of the sawtooth heat pulse in the edge is strongly correlated with a following or concurrent sharp decrease in LFEO frequency. The frequency then slowly increases before either reaching a plateau or the next sawtooth heat pulse arrives. This cycle gives the LFEO a chirping frequency structure.

We can assess if this is consistent with GAM theory by inspecting the edge electron temperature response to the sawtooth heat pulse. In Figure 7c and Figure 7d we plot the pedestal electron temperature, for AUG and C-Mod respectively, and compare it to the experimentally observed LFEO frequency (Figure 7e and Figure 7f) since ($f_{GAM} \propto \sqrt{T_e}$).

On AUG, we use two ECE channels for this analysis. The first is the channel near $\psi_n \approx 1$, near where we expect the LFEO to be driven. We use this channel to measure the LFEO frequency. However, as the optical thickness is well below 2 at this point in the plasma, we cannot use this channel to measure temperature. The second channel is located about $\psi_n = .95$ (half way up the pedestal) and is the first channel where the optical thickness is above 2. We use this channel to get a time history for the electron temperature to qualitatively compare LFEO frequency and GAM theory.

On C-Mod, the channel measuring the top of the pedestal, around $\psi_n \approx .96$, is used for both temperature measurement and LFEO frequency measurement. This was the last channel we were confident was inside of the LCFS.

On AUG the pattern is clear: The electron temperature falls sharply after the initial spike from the sawtooth heat pulse, consistent with the reduction in LFEO frequency. As the temperature subsequently increases, so does the experimental LFEO frequency. This is the behavior we would expect of a GAM! It is unclear why the electron temperature drops so sharply following the sawtooth heat pulse. One possibility is that the heat pulse causes additional ionization in the pedestal near the LCFS which act as an inward propagating cold pulse, another possibility is that the heat pulse transiently alters the electron temperature gradient to increase thermal transport leaving a “hole” in the electron temperature profile. Investigating this phenomenon is left to future work.

On C-Mod the pattern is less clear, we see the decrease in LFEO frequency shortly following the sawtooth crash similar to AUG (albeit a little delayed). In general, the LFEO frequency and temperature follow a similar drop off and recovery pattern as seen on AUG, however the timing is not exact, and the temperature recovery is not as strong as seen on AUG. We suspect this is due to the necessity of using a pedestal top ECE channel. In the highly collisional edge of C-Mod a local cold plasma source (such as bulk ionizations of edge neutrals due to the sawtooth pulse) may not reach the pedestal top. Nonetheless, the reduction in LFEO frequency with the decay of the sawtooth pulse is consistent with GAM theory and gives support to the hypothesis (or identification) that the LFEO is a GAM.

The small timing differences in when the LFEO frequency decreases in response to the sawtooth between C-Mod and AUG can be explained by error introduced by the spectral analysis technique. We calculated the instantaneous frequency at each point using a short time Fourier transform ($8.2ms$ window for C-Mod, $32.7ms$ window on AUG) which introduces a temporal blurring effect on the order of the window size. Thus, the timings of the shifts in frequency have an error of about half the window size associated with them. Using two different locations on AUG for the electron temperature and LFEO could also introduce the timing issues.

4.5 Fluctuation Amplitude

We use the FRC-ECE to determine the temperature fluctuation amplitude on C-Mod by taking the RMS value of the temperature after applying a narrow bandpass filter around the LFEO frequency. In the channel at $\psi_n = .964$, near the pedestal top, we find $\tilde{T}_e/T_e = 0.005$ with an absolute $\tilde{T}_e \sim 5eV$. This stands in stark contrast with the major temperature fluctuation seen in the ETRO at EAST, which is reported to be about $\tilde{T}_e/T_e \sim .09$ at the top of the pedestal. $\tilde{T}_e/T_e = 0.005$ near the midplane is more consistent with the $m = 1$ GAM than with the $m = 0$ ETRO which should have a similar fluctuation amplitude wherever we measure it. We will see in the next section that the LFEO relative electron temperature fluctuation can be an order of magnitude larger near the foot of the pedestal, which would put it within a factor of two of the ETRO, albeit in an inconsistent location.

5. Radial Structure and Propagation

We have investigated the radial structure of the LFEO on C-Mod using a combination of GPI and the MLP. Neither diagnostic can detect the radial structure alone, however, by phase locking the moving MLP measurements to a stationary GPI channel, a novel analysis technique reveals the radial structure. The MLP and GPI systems are shown in Figure 8.

5.1 Coupling Method

The MLP scans from the SOL to just inside of the LCFS and makes measurements of electron density, temperature, and electric potential with a sampling frequency of $1.1MHz$. However, the spatial and temporal information are inherently coupled. In order to take advantage of the high spatial and temporal resolution of the MLP, we use the GPI signal as a reference clock to perform a phase locking analysis. To explain this method, we consider the LFEO as a radially propagating plane wave with real frequency $f_0 = 1/T_0$ and wave length λ_0. Let the stationary GPI chord be at position $x_{GPI} = 0$ and the starting position of the probe be $\rho_{MLP} = \rho_0$. At time $t = 0$ the GPI signal will be at a maximum ($n_{GPI} = n_0$), and the MLP signal will be:

$$n_{MLP,0} = n_0 \cos\left(2\pi \frac{\rho_0}{\lambda_0}\right) \tag{6}$$

In other words, the probe signal will be phase shifted by $2\pi \frac{x_0}{\lambda_0}$. At the future time $t = T_0$ the GPI will still see $n_{GPI} = n_0$ and the MLP will measure:

$$n_{MLP,0} = n_0 \cos\left(2\pi \frac{\rho_0 + v_{MLP} T_0}{\lambda_0}\right) \tag{7}$$

The phase shift has changed by a factor of $2\pi v_{MLP} T_0/\lambda_0$. Thus, if we only take MLP data points collected when the GPI signal reaches a local maximum, the LFEO wave form is sketched out. This procedure can be seen in Figure 9 for simulated data. The simulation injected a plane wave propagating in the same direction as the probe motion across the entire simulation domain.

Since this procedure is fundamentally measuring the phase shift of the MLP compared to the GPI, we are not limited to only taking points when GPI is at maximum, but may take any set of points where GPI

is at the same phase (ϕ_{GPI}). In fact, this analysis can be used for non-sinusoidal waveforms, as long as they are periodic. Further, this result is not impacted by the addition of poloidal propagation in simulations; only the radial wave structure is measured.

One can think of this method as creating an array of "virtual" Langmuir probes with radial spacing equal to $\Delta\rho = v_{MLP}/f_{LFEO}$. This allows us to write a Nyquist condition on spatial sampling:

$$\frac{\omega_{LFEO}}{v_{MLP}} \pm k_{LFEO} \geq 2k_{LFEO} \tag{8}$$

where the $\pm k_{LFEO}$ accounts for the doppler shift of the probe frequency for a wave moving against probe motion (+) or with probe motion (-). If the LFEO is a standing wave, the Doppler shift term is ignored. The relationship between the LFEO frequency and minimum detectable wavelength is displayed in Figure 10 for a probe velocity of $v_{MLP} = 1\,m/s$, which is a reasonable value close to the end of the probe plunge. For LFEO frequencies of interest, the minimum detectable wavelength is less than 0.33mm.

A more stringent limit on the minimum detectable wavelength is given by the GPI spot size. The GPI spot size of 3.8mm means that any fluctuation with wavelengths near or below that value will be attenuated. This method requires information about the phase of the GPI signal and not the magnitude, therefore as long as the signal to noise ratio remains high enough to be detected, the LFEO can be detected. The LFEO's apparent amplitude in GPI would be smaller than the actual amplitude in this case. This issue is alleviated somewhat by integrating over several GPI channels in a vertical column to improve signal to noise. In this work, we integrate the top four rows in the third column from the left in Figure 8. In practice, this sets the minimum detectable wavelength around 1mm as long as $3.8mm \bmod \lambda \neq 0$ to ensure the signal will not be attenuated too much.

5.2 Coupling Results

The MLP was inserted into C-Mod shot 1150916025 during a stable I-Mode in LSN and unfavorable grad-B drift configuration. The plasma conditions during the probe plunge were generally stable, with ICRH heating power (Figure 11a) of 1.5MW, line averaged density (Figure 11b) of $1.1 * 10^{20} m^{-3}$ measured by Two Color Interferometry, and core temperature (Figure 11c) around $2\ keV$. This shot had an unusually low magnetic field and current (for C-Mod) of 2.8T and 550kA respectively. These conditions were chosen to reduce L-I threshold power and thus heat load on the MLP, allowing it to scan past the LCFS. A strong LFEO centered around 17kHz is observed in Divertor Langmuir probe currents (Figure 11d) and confirmed in pedestal reflectometry during the duration of the probe plunge.

The results of the phase locking analysis are shown in Figure 12. A clear oscillatory structure is observed in plasma potential (Figure 12a) when the GPI phase is 180^0, with a fluctuation amplitude of 5V and wavelength of 1.6mm. The pattern is reversed in the 0^0 GPI phase electric potential profile, reaching a peak value at roughly the same location as the minimum in the 180^0 profile. Intermediate phase channels also show the structure, although not as clearly. This feature is not seen clearly in the temperature profiles (Figure 12b) with only a small dip in the 180^0 profile, suggesting the presence of the LFEO. However, it is clearly present in the density fluctuation (Figure 12c) with an obvious separation

of the 0^0 and 180^0 profiles and fluctuating density amplitude of . $125 * 10^{20} m^{-3}$. Electron temperature from a two-point power balance model [68] places the LFEO structure just inside the LCFS, with some of the fluctuation structure existing in the SOL. This may account for the presence of the LFEO on the divertor Langmuir probes.

Each data point in Figure 12 is calculated using an 11^ophase window over which we average the MLP measurment. As we are using data from a single diagnostic, any systematic error will be constant over the course of the probe plunge, thus only random errors in the I-V fitting routine and electronic noise need to be considered to ensure. The error bars are the standard error calculated at each point over phase window.

These fluctuation amplitudes can be compared to those predicted theoretically for the GAM. The experimental fluctuation density is $\tilde{n}_{e,exp}/n_0 = 0.1$ (half peak to peak). Taking $T_e = 72eV, \theta = 32^o, \lambda = 1.6mm$, and a deuterium plasma as inputs to Equation 4, we find the theoretical density fluctuation for a GAM to be $\tilde{n}_{e,theory}/n_0 = 0.165$. The theoretical density fluctuation slightly overpredicts the experimental one. However, given the high level of signal processing that was needed to get the fluctuating potential and density profiles and the fact that Equation 4 was derived assuming no temperature fluctuation and for a circular cross section, the agreement is quite close.

No simple estimate exists for theoretical temperature fluctuation amplitude, preventing us from comparing experiment and theory for temperature fluctuations. However, the temperature fluctuation has a magnitude (half of the maximum separation in Figure 12b) of $T_e \sim 2.5eV$ and $\tilde{T}_e/T_e \approx 0.04$ which is consistent with the RMS fluctuation level in the raw MLP signals. The relative amplitude is significantly larger than what we see in ECE (Section 4.5), however, that measurement was made near the top of the pedestal where the average temperature is much higher. AUG measurements suggest this has a lower amplitude than further out in the pedestal (Figure 4). The absolute fluctuation is similar in both measurements.

It is worth comparing the measured LFEO fluctuation levels to the fluctuation levels measured for the Quasi Coherent Mode (QCM) thought to be responsible for regulating impurity accumulation in EDA H-Mode. Using the same MLP diagnostic, Labombard et al [19] showed that the QCM had a half peak to peak density fluctuation of $\tilde{n}_{e,exp}/n_0 = 0.15$ and temperature fluctuation of $\tilde{T}_e/T_e \approx 0.225$. The fact that the density and temperature fluctuations are larger and that $\tilde{T}_e/T_e > \tilde{n}_e/n_e$ for the QCM gives us confidence that the MLP can measure a wide range of plasma fluctuations, including those for the LFEO. It also gives us confidence that the LFEO is a fundamentally different mode than the QCM, which has qualities consistent with an electron drift wave [19].

The radial electric field caused by the LFEO potential perturbation is roughly $\tilde{E} = 12.5\, kV/m$ which would produce a poloidal EXB velocity of $\tilde{v}_\theta = 4.4\, km/s$. This is consistent with prior measurements of the GAM velocity in C-Mod using Time Delay Estimation analysis for the GPI system performed by Cziegler et. al. [16] where it was found the GAM had a poloidal velocity of $\tilde{v}_\theta = 2.2\, km/s$ which gave an electric field of $\tilde{E} = 10\, kV/m$. If the LFEO is a GAM, the difference in velocity is well explained by the lower magnetic field strength in the shot analyzed here, by nearly a factor of 2, compared to the shot analyzed by Cziegler et. al. ; ExB velocity would be lower for constant E.

The direct analysis of the LFEO electric field fluctuation, GAM like relationship between density perturbation and poloidal flow structure are the strongest evidence presented for the LFEO being some kind of GAM.

It should be noted that our observed wavelength is on the scale of typical ion turbulence wavelength and thus models of GAM turbulence coupling that rely on scale seperation do not apply. Any model for how the GAM is modifying turbulant transport would need to include these scales.

5.3 Radial Propagation

A major unanswered question is whether or not the LFEO is a propagating or standing wave. This can be investigated by examining the relationship between the GPI phase and the phase of the resulting phase locked MLP profile. Any given phase locked MLP profile can be roughly modeled using:

$$S_{MLP}(\rho) = A\cos\left(2\pi\frac{\rho}{\lambda} + \alpha\right) + f(\rho) \tag{9}$$

where A is the LFEO amplitude, α is a phase shift related to the distance between the GPI and our zero point (in this case the position of the LCFS) and to the GPI phase (ϕ_{GPI}), and $f(\rho)$ is the background profile without the LFEO present.

It is the relationship between α and ϕ_{GPI} that allows us to measure propagation. ϕ_{GPI} becomes a time proxy. As we increase ϕ_{GPI}, the resulting LFEO wave will be shifted either left or right depending on its propagation direction. In the phase locked MLP profiles, this is equivalent to the *spatial* phase shift (i.e. α in Equation 9). If the wave is propagating to the right (outward), then this will appear as a decrease in α (e.g. $\alpha \propto -\phi_{GPI}$) and if the wave propagates to the left (inwards), it will appear as an increase in α (e.g. $\alpha \propto \phi_{GPI}$). If the LFEO is a standing wave, α will be independent of ϕ_{GPI}, except for an abrupt 180^o phase shift to account for the need for the first term in Equation 9 to describe a standing wave without a second trigonometric term. It should be noted that this behavior holds true regardless of the direction of probe motion.

We perform this analysis for shot 1150916025 by generating a large number of phase locked profiles with ϕ_{GPI} from $0 \rightarrow 360^o$ in steps of 3.6^o with an averaging window of 3.6^o (i.e. all of the data collected by the probe was used). $f(\rho)$ is calculated by averaging all of the phase locked profiles. We then subtract $f(\rho)$ from the individual phase locked profiles and window the remaining data down to $-3.4mm < \rho < -1.5mm$. Finally, we fit each mean subtracted phase locked profile with:

$$S_{MLP}(\rho) = A\cos\left(2\pi\frac{\rho}{\lambda} + \alpha\right) + c \tag{10}$$

where we take $\lambda = 1.6mm$ and allow A, α and c to be fitting parameters. c is a constant offset that is included to improve the quality of the fits.

We plot the αs obtained from fitting equation 10 to the plasma potential profiles against ϕ_{GPI} in Figure 13a. The R^2 values for each fit are plotted in Figure 13b. We have removed fits with $R^2 < .5$, which mostly cluster around the times when the MLP shows flatter profiles. Including the poorer fits does not much change the final result. It is immediately clear that the LFEO is a wave that is propagating radially

inward. This is consistent with theoretical models of an inwardly propagating GAM [51], that predict the potential and density being in phase above the outer midplane. The same theory predicts an outwardly propagating GAM would be temporally 180^o out of phase above the outer midplane.

6. Comparison of the LFEO, GAM, and ETRO

A major question of this study is: what is the relationship between the LFEO, GAM, and ETRO? In this section we compare the LFEO to both GAM theory and the experimental characterization of the ETRO carried out by Liu et. al. [17,18].

6.1 Localization

The LFEO and ETRO have been localized to two different, albeit overlapping regions. The LFEO has been shown to primarily exist in the steep pedestal region or near the pedestal foot on both AUG and C-MOD (Figure 3). While the LFEO extends to the top of pedestal it does not appear much deeper in the core, and is strongest near the separatrix. The ETRO is reported to have the opposite behavior. It peaks above the top of the pedestal, persists deeper into the core, and decays rapidly in the pedestal. This would indicate that the ETRO and LFEO are probably not the same mode.

6.2 Magnetic Mode Number

The LFEO has been shown to have a $n = 0, m = 2$ magnetic structure. This is consistent with GAM theory. The ETRO has been shown to have a $n = 0, m = 1$ magnetic structure which is inconsistent with both GAM theory and the LFEO. This again points to the LFEO and the ETRO being different modes.

6.3 Frequency

The LFEO and the ETRO are very close to one another in frequency space. While on C-Mod, the LFEO frequency tended to be quite a bit higher ($10 - 30\ kHz$) than the ETRO ($\sim 8\ kHz$), the LFEO on AUG ($7 - 12\ kHz$) is right in line with ETRO frequencies. Given the size difference between C-Mod ($R = .67m$), AUG ($R = 1.65m$), and EAST ($R = 1.7m$ [69]) and the strong R^{-1} scaling in the GAM frequency, the LFEO and the ETRO live in a nearly identical frequency range across all machines (assuming the LFEO is a GAM). As we have seen, this is consistent with a GAM driven near the LCFS, however as the ETRO does not live in that region, it will experience different "drive conditions" than the LFEO. This suggests that the LFEO and ETRO frequencies have different dependencies on local plasma conditions (or at least some kind of scale factor). This again points to the ETRO and LFEO being different modes.

6.4 Fluctuation Amplitudes

The strongest evidence that the LFEO and ETRO are different modes is the difference in their fluctuation amplitudes. The ETRO and LFEO both have observed temperature and density fluctuations. The ETRO has $\tilde{T}_e/T_e \sim .09$ and $\tilde{n}_e/n_e < .02$ [17]. The dominance of the ETRO temperature fluctuation is where it draws its name. However, as we have seen the LFEO has a very small temperature fluctuation at the top of the pedestal $\tilde{T}_e/T_e \sim 0.005$, and only reaches $\tilde{T}_e/T_e \approx 0.04$ at the foot of the pedestal where it is at its maximum. The LFEO is primarily a density fluctuation $\tilde{n}_e/n_0 = 0.1$. Again, the LFEO and ETRO have

opposite characteristics. The fluctuation amplitude characteristics of the LFEO are consistent with a GAM, the fluctuation characteristics of the ETRO seem not to be.

6.5 The LFEO is not the ETRO

A major conclusion of this paper is that the LFEO observed on C-Mod is likely not the ETRO observed on EAST. In every compared category except for frequency, the C-Mod LFEO and the ETRO exhibit quite different behavior. While the LFEO on AUG has not been as thoroughly explored, its similar location near the middle/foot of the pedestal and similar chirping behavior in response to the sawtooth crash would suggest that it is the same mode as the C-Mod LFEO.

6.6 The LFEO is likely a modified propagating eigenmode GAM

The second major conclusion of this paper is that the C-Mod LFEO and likely the AUG LFEO are modified propagating eigenmode GAMs. This conclusion is supported by the LFEO's $m = 2$ poloidal magnetic structure, frequency scaling with $\sqrt{T_e}$ and absolute frequencies within a factor of two or three of the GAM, and our direct measurement of the LFEO's density and radial electric field fluctuations and propagation. We say "modified" because it is clear that something not captured in kinetic GAM theory is reducing the GAM frequency. Theory has shown that including a finite plasma rotation can induce a second, lower frequency GAM [47,70,71], which is a possible explanation for this modification. However, further experiments would be necessary to assess if that is the modification mechanism here.

6.7 Role of the LFEO and ETRO

While we have concluded that the LFEO and ETRO are not the same mode, they may play a similar role in I-Mode physics. The ETRO is thought to mediate a rapid switching between TEM and ITG turbulence. It is this rapid switching that is thought to lead to the distinctive I-Mode transport properties on EAST. It is possible, although we have not tested this hypothesis, that the LFEO, through oscillating shear suppression, could mediate a similar rapid transition between TEM and ITG on C-Mod and AUG. Further experiments would be needed to show this rapid turbulence transition exists.

It should be reiterated that we have not established that the LFEO is a ubiquitous feature of I-Mode. Thus, we make no claim that the LFEO is necessary for I-Mode physics, only that it may modify the transport when present.

7. Summary

The I-Mode confinement regime [2] is an exciting prospect for a potential future fusion reactor due to its high energy confinement, low impurity confinement, and stability against edge localized modes. However, the physics behind it is largely not well understood. One of the key open questions regarding I-Mode is how the energy and particle transport become uncoupled, such that the former is low and the latter is high. It has been proposed that low frequency fluctuations could moderate transport and lead to the separation of transport channels.

Thus, we carried out an extensive investigation of the characteristics of the LFEO and compared it to GAM theory and to the ETRO on EAST to better understand the low frequency fluctuations in I-Mode.

From this investigation, we came to two conclusions: The LFEO on C-Mod and likely AUG is a modified propagating eigenmode GAM, and that the LFEO and ETRO are likely different modes.

Acknowledgement

The authors sincerely thank Istvan Zeigler and Peter Manz for many valuable discussions regarding prior analysis of the I-Mode GAM on C-Mod and AUG respectively and Ahdi Liu for clarifications regarding the flux coordinate used on EAST. Work related to C-Mod was supported by US DOE Award DE-SC0014264. Work related to ASDEX Upgrade has been carried out within the framework of the EUROfusion Consortium, funded by the European Union via the Euratom Research and Training Programme (Grant Agreement No 101052200 - EUROfusion). The views and opinions expressed are however those of the authors only and do not necessarily reflect those of the European Union or the European Commission. Neither the European Union nor the European Commission can be held responsible for them. Some of the analysis work was carried out under NRC grant 31310021M0034.

Conflict of Interest

The authors have no conflicts to disclose.

Data Availability

The data that support the findings of this study are available from the corresponding author upon reasonable request.

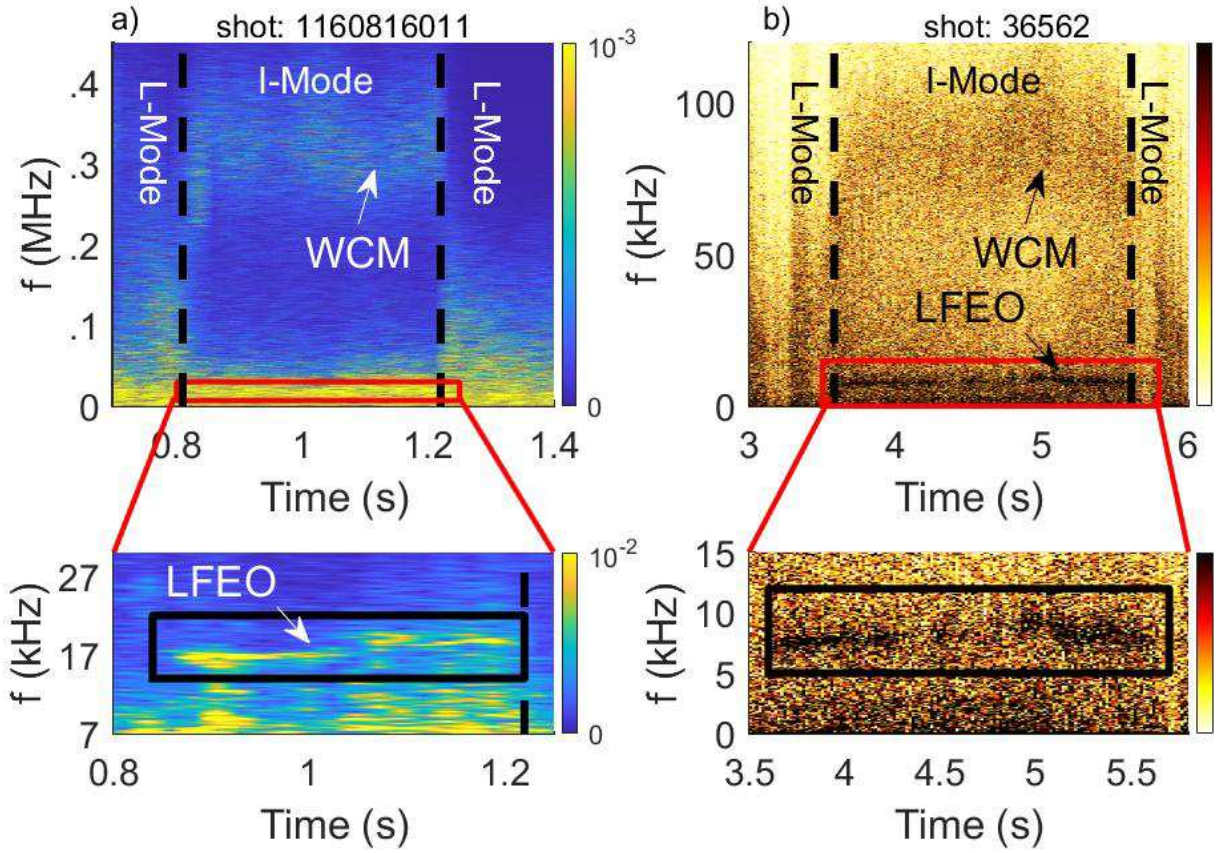

Figure 1 – *The spectral structure of the density fluctuations in the pedestal of I-Mode on a) C-Mod and b) AUG as measured in the conventional reflectometer amplitude. The clear band around a) 350 kHz and b) 80kHz is referred to as the Weakly Coherent Mode. A second fluctuation (within black box) around a) 17 kHz and b) 8 kHz is referred to as the Low Frequency Edge Oscillation.*

Parameter	**Symbol**	**C-Mod** [20]	**AUG** [29]	**Unit**
Major Radius	R	.67	1.65	m
Minor Radius	a	.22	.5	m
Toroidal Field	B_T	2.4-8.1	<3.4T	T
Plasma Current	I_p	.24-2.0	<1.4	MA
Average density	n_e	.2-8.0	1	$10^{20}/m^{-3}$
Central Electron Temperature	T_e	<9	<15	keV
ICRH Power	P_{ICRH}	5	6	MW
ECRH Power	P_{ECRH}	0	6.4	MW
NBI Power	P_{NBI}	0	20	MW

***Table 1**- Machine parameters of Alcator C-Mod and ASDEX Upgrade*

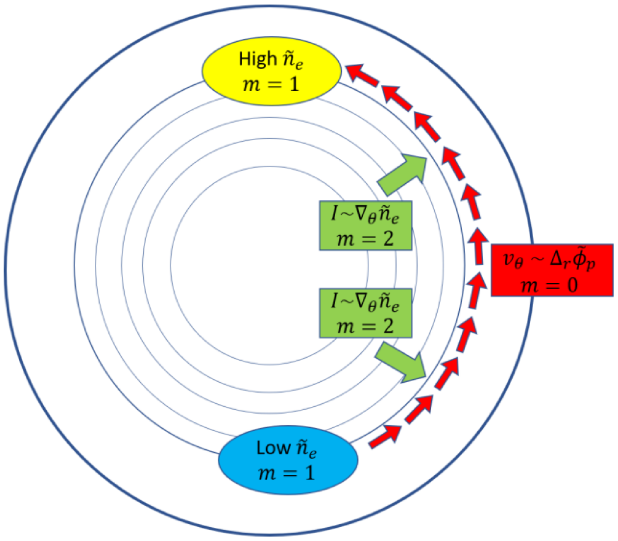

Figure 2 – *The Geodesic Acoustic Mode structure depicting the m=0 poloidal flow perturbation that results from the radial potential perturbation, the resulting the m=1 density/pressure perturbation, and the m=2 current perturbation that results in the magnetic field perturbation.*

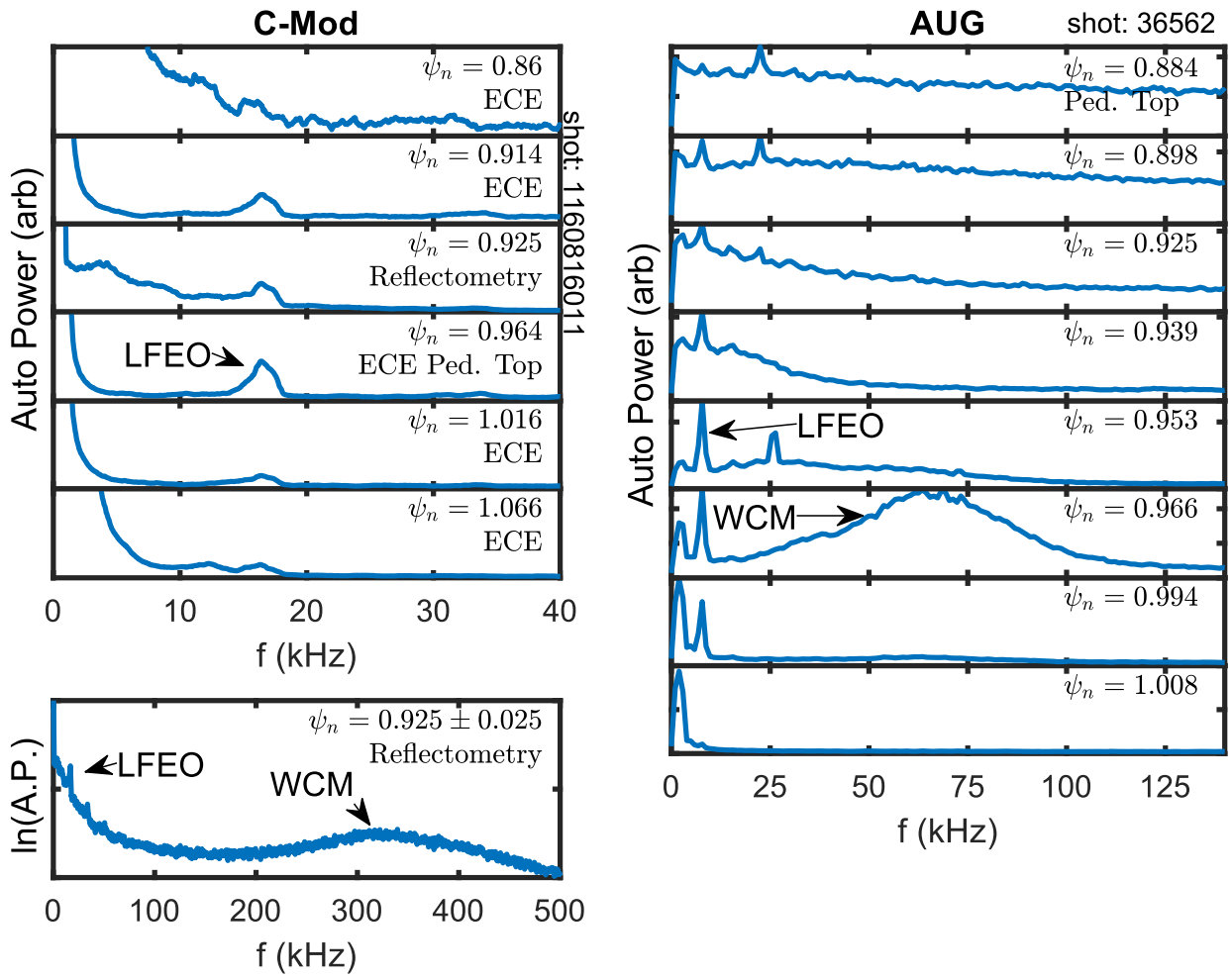

Figure 3 *–The Location of the LFEO on C-Mod is determined by inspecting the Auto Power estimate of FRC-ECE and Reflectometry channels in the edge region. The LFEO is present in the ECE channels at the top of the pedestal (ψ_n = .964) and on the channel immediately outside the LCFS, although that channel is optically thin and its integration width includes part of the pedestal. The edge reflectometry channel shows both the LFEO and WCM slightly above the pedestal top, however the LFEO's large density fluctuation introduces error in the localization of that channel. On AUG the CECE diagnostic shows the LFEO spanning from the foot of the pedestal to the top of the pedestal with the WCM appearing in a channel near the pedestal foot.*

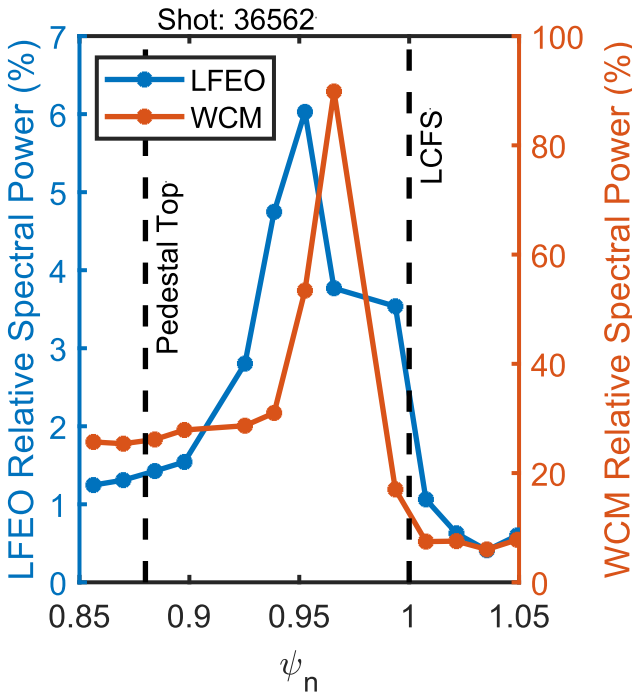

Figure 4 – *The spectral power contained in the LFEO and WCM frequency bands (relative to the total spectral power in the signal) in the CECE channels spanning the pedestal on AUG.*

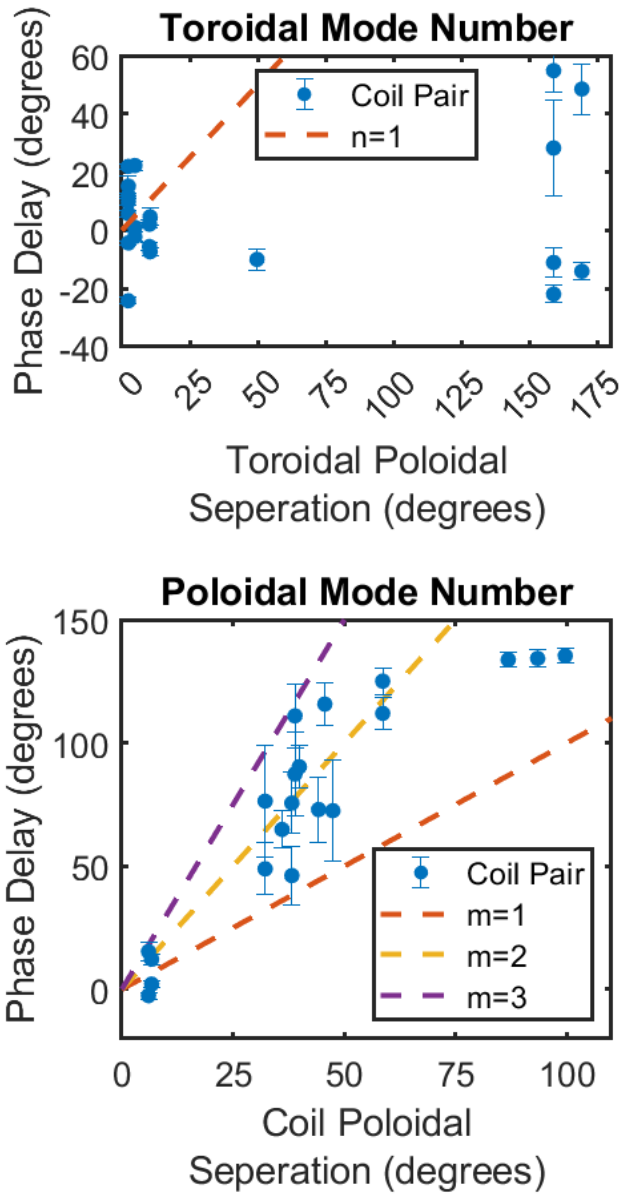

Figure 5 *–The magnetic mode number analysis carried out on C-Mod shot 1160804002. The phase delay was calculated using pairs of coils and plotted against the angular separation between the coils. Each point represents a unique coil pair. The m=1,2,3 mode numbers are shown as the dashed lines. The absolute value of cross phase and coil separation has been plotted for ease of interpretation.*

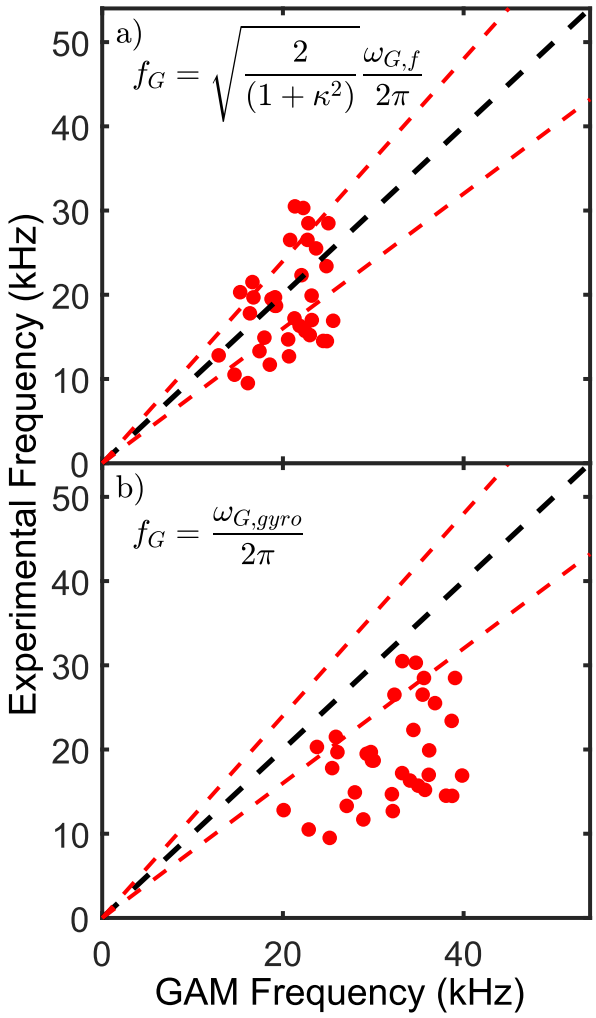

Figure 6 – *Two GAM frequency scalings are evaluated on C-Mod. Temperatures at the 98% flux surface are used as they provide the best fit to a* $\sqrt{T_e}$ *trend. The modified fluid scaling is shown in a). The gyrokinetic scaling is shown in b) for an elongation of 1.6 as measured by EFIT.*

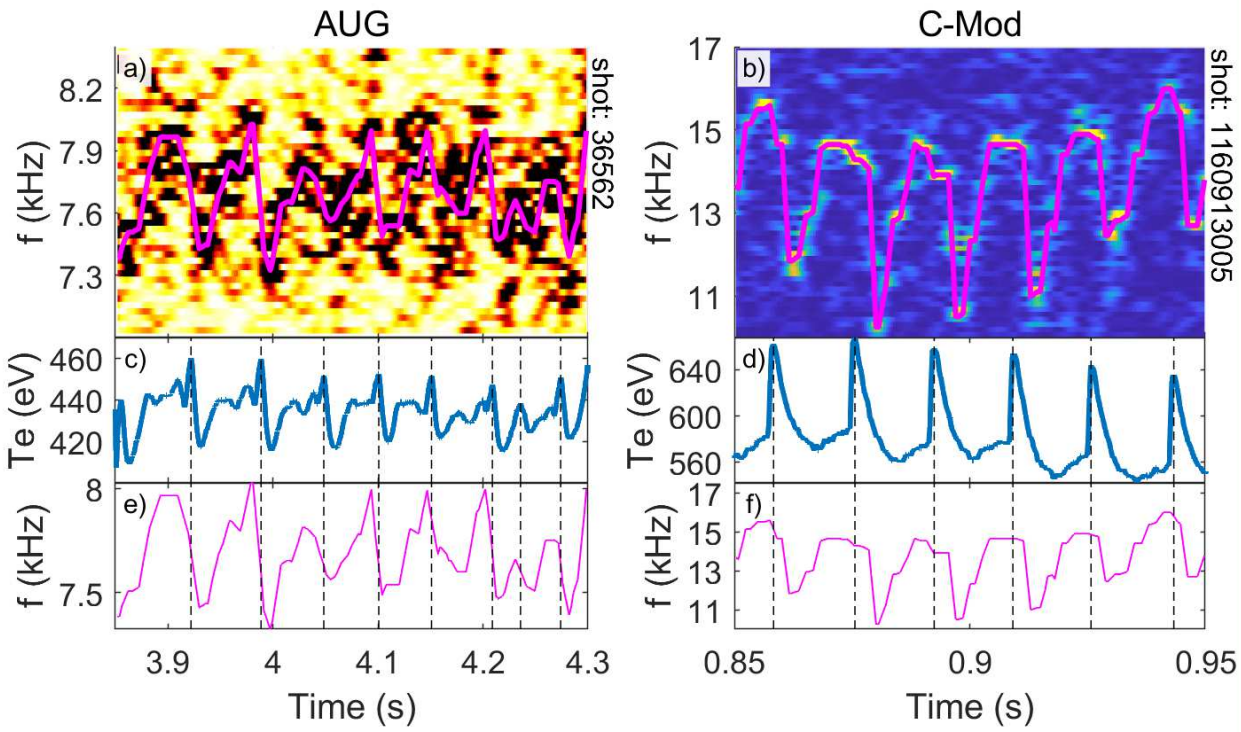

Figure 7 *–The AUG temperature fluctuations, a), and C-Mod temperature fluctuations, b) shows the sawtooth modulation of the LFEO. The magenta line traces the frequency of maximum spectral power. Edge temperatures measured by ECE on both machines, c) and d) show the reduction in edge temperature following the sawtooth heat pulse. The temporal evolution of the experimental LFEO frequencies, e) and f), show a similar pattern to the electron temperature.*

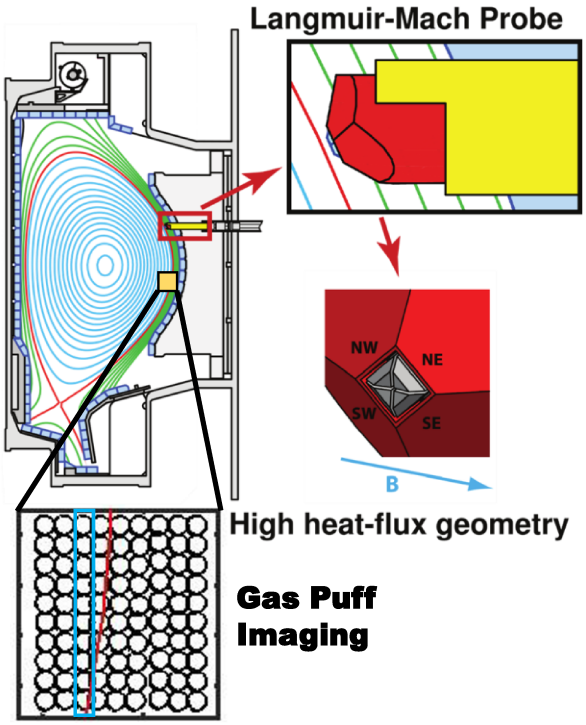

Figure 8 – *Schematic of the scanning Mirror Langmuir Probe which provides high time resolution measurements of density temperature and potential above the outer midplane. Also shown is the viewing area of the Gas Puff Imaging diagnostic (yellow box is approximate area only). The blue box is the GPI channel used in Section 5.*

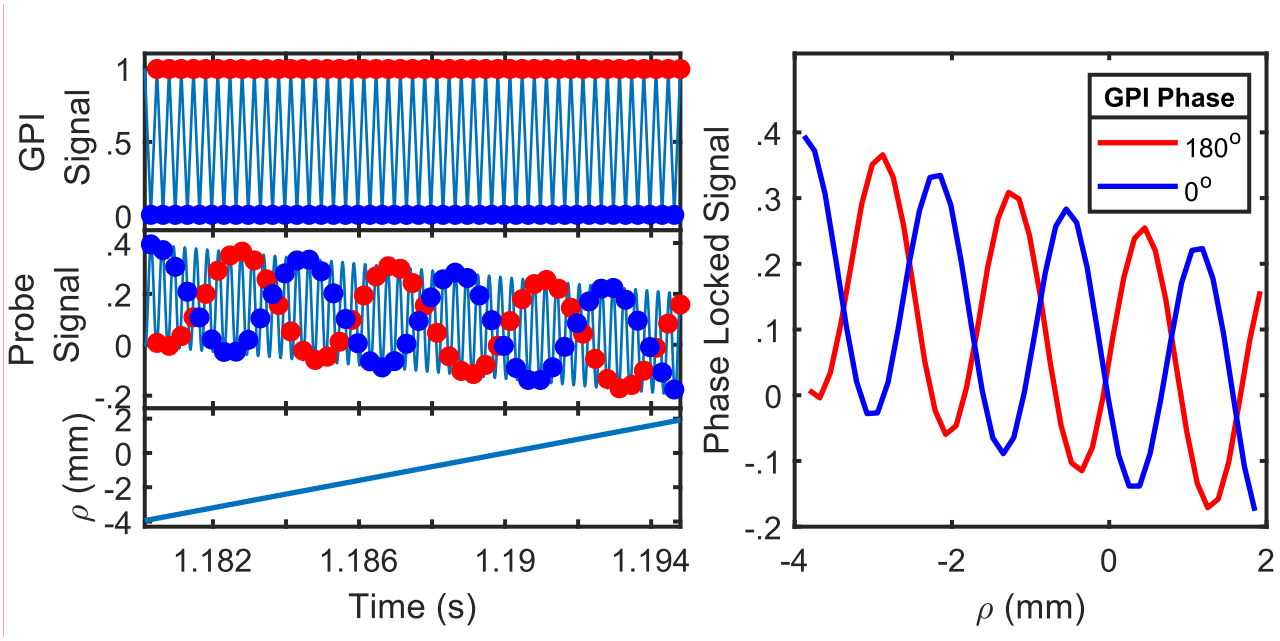

Figure 9 – *An example of the MLP-GPI phase locking procedure from a simulated LFEO wave launched into the measurement region. Times where the GPI signal reaches a maximum (minimum) are marked with red (blue). Due to the probe's motion, it measures a different location each time the GPI is at a constant phase. This results in the LFEO wave form beina sketched out.*

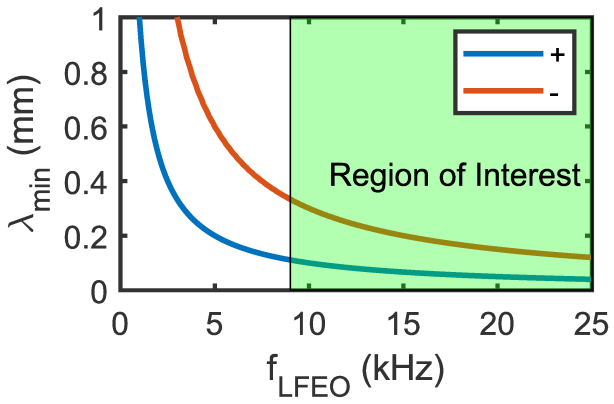

Figure 10 – *The minimum wavelength that is detectable by the MLP GPI coupling is based on the frequency of the LFEO and the relative velocity of the wave of the probe. The region with observed LFEO frequencies is highlighted in green. The + (-) branch is for the LFEO and probe moving towards (away from) each other.*

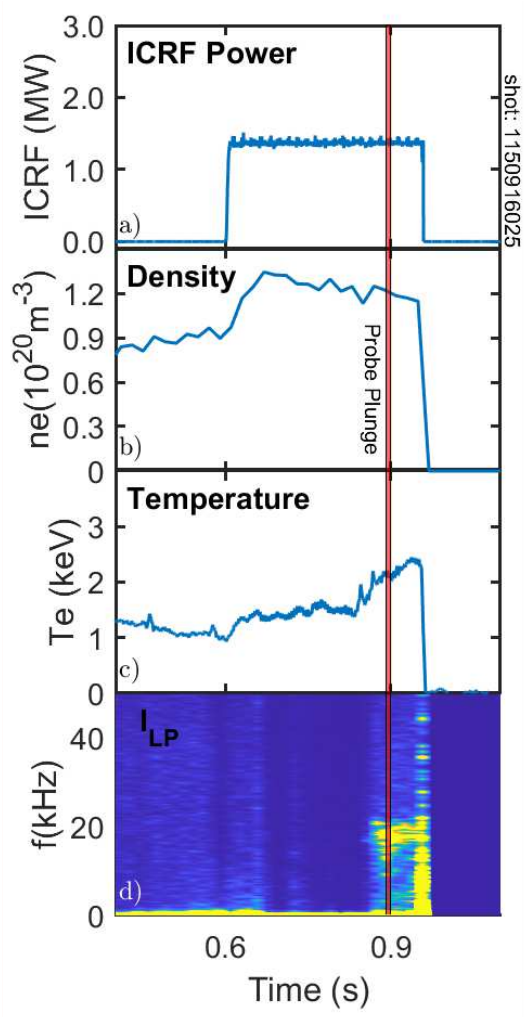

Figure 11 *– The probe plunge occurs during a period of stable ICRF power a), stable line averaged electron density b), temperature c), and LFEO frequency d).*

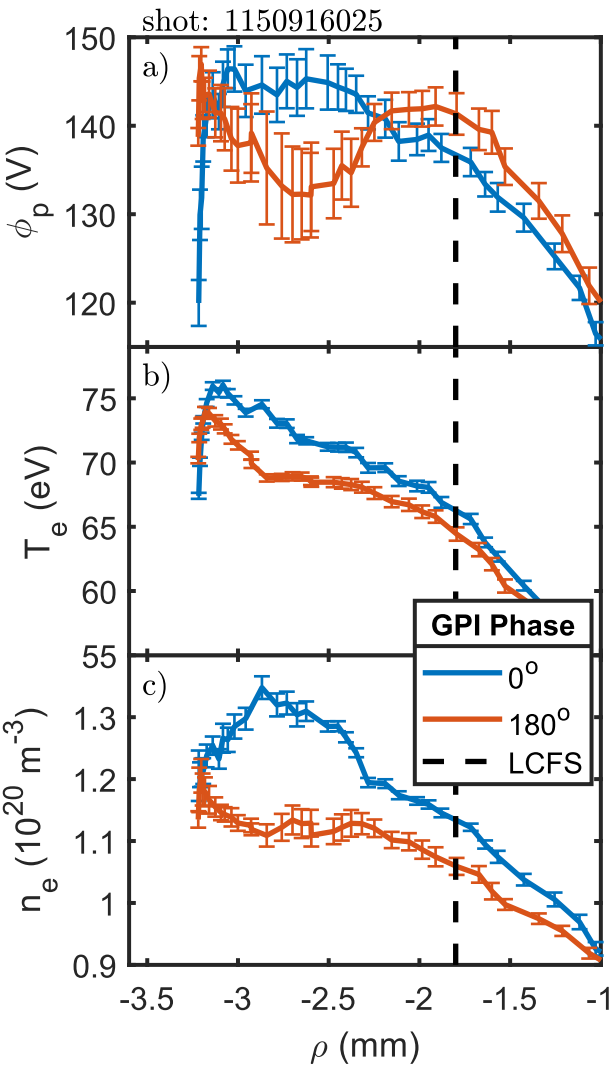

Figure 12 *– The phase locked MLP Plasma Potential a), electron Temperature b), and electron density c). GPI Phase is the constant phase used to phase lock the MLP signals. A GPI phase of 0 and 180 should show inverted wave forms for a wave structure, which is observed.*

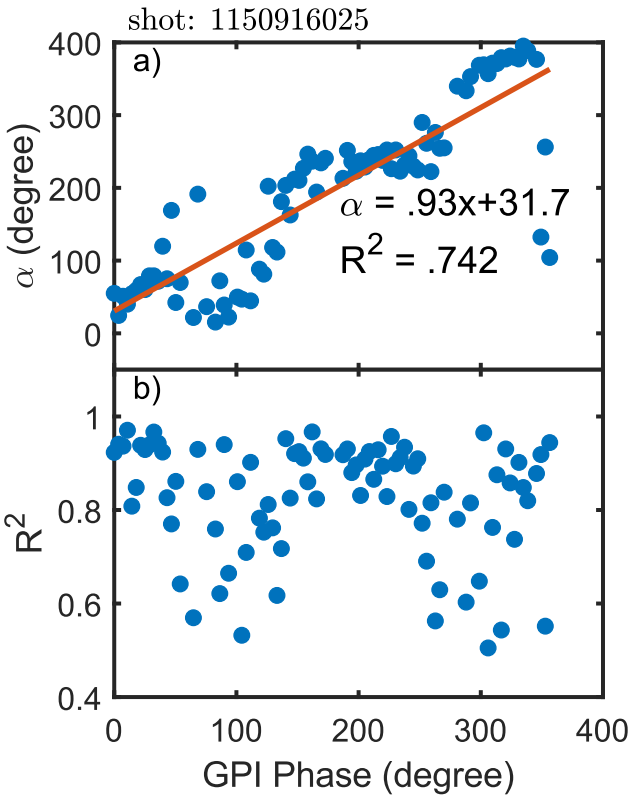

Figure 13 – *The investigation of LFEO propagation reveals inward propagation. In a) the fitted spatial phase shift is plotted against the GPI phase of the fitted phase locked profile. In b) the R^2 value of the fit is shown.*

Bibliography

[1] F. Wagner, *A Quarter-Century of H-Mode Studies*, in *Plasma Physics and Controlled Fusion*, Vol. 49 (2007).

[2] D. G. Whyte et al., I-mode: An H-mode energy confinement regime with L-mode particle transport in Alcator C-Mod, Nuclear Fusion **50**, (2010).

[3] A. E. Hubbard et al., Physics and performance of the I-mode regime over an expanded operating space on Alcator C-Mod, Nuclear Fusion **57**, (2017).

[4] P. Manz et al., Geodesic oscillations and the weakly coherent mode in the I-mode of ASDEX Upgrade, Nuclear Fusion **55**, (2015).

[5] F. Ryter et al., H-mode power threshold and transition in ASDEX Upgrade, Plasma Phys Control Fusion **40**, 725 (1998).

[6] M. Greenwald, J. Scharchter, W. Dorland, R. Granetz, A. Hubbard, J. Rice, J. A. Snipes, P. Stek, and S. Wolfe, Transport phenomena in Alcator C-Mod H-modes, Plasma Phys. Control. Fusion **40**, 789 (1998).

[7] T. Happel et al., Stationarity of I-mode operation and I-mode divertor heat fluxes on the ASDEX Upgrade tokamak, Nuclear Materials and Energy **18**, 159 (2019).

[8] J. Chen, D. Brower, J. McClenaghan, Z. Yan, A. E. Hubbard, and R. Groebner, Turbulence link to L-mode, I-mode, and H-mode confinement in the DIII-D tokamak, Nuclear Fusion **64**, (2024).

[9] X. Feng et al., I-mode investigation on the Experimental Advanced Superconducting Tokamak, Nuclear Fusion **59**, (2019).

[10] J. R. Walk et al., Edge-localized mode avoidance and pedestal structure in I-mode plasmas, Phys Plasmas **21**, (2014).

[11] T. Happel et al., The I-mode confinement regime at ASDEX Upgrade: Global properties and characterization of strongly intermittent density fluctuations, Plasma Phys Control Fusion **59**, (2017).

[12] D. Silvagni et al., I-mode pedestal relaxation events in the Alcator C-Mod and ASDEX Upgrade tokamaks, Nuclear Fusion **62**, 036004 (2022).

[13] D. Silvagni et al., I-mode pedestal relaxation events at ASDEX Upgrade, Nuclear Fusion **60**, (2020).

[14] M. Herschel, T. Happel, D. Wendler, M. Griener, J. Kalis, R. Fischer, P. Manz, and U. Stroth, Experimental evidence for the drift wave nature of the weakly coherent mode in ASDEX Upgrade I-mode plasmas, Nuclear Fusion **64**, (2024).

[15] W. C. Mccarthy, The Low Frequency Edge Oscillation in Alcator C-Mod and ASDEX Upgrade I-Mode, Massachusetts Institute of Technology, 2022.

[16] I. Cziegler et al., Fluctuating zonal flows in the I-mode regime in Alcator C-Mod, Phys Plasmas **20**, (2013).

[17] A. D. Liu et al., Experimental identification of edge temperature ring oscillation and alternating turbulence transitions near the pedestal top for sustaining stationary I-mode, Nuclear Fusion **60**, (2020).

[18] A. D. Liu et al., Characteristics of the edge temperature ring oscillation during stationary improved confnement mode in EAST, (2023).

[19] B. LaBombard, T. Golfinopoulos, J. L. Terry, D. Brunner, E. Davis, M. Greenwald, and J. W. Hughes, New insights on boundary plasma turbulence and the quasi-coherent mode in Alcator C-Mod using a Mirror Langmuir Probe, Phys Plasmas **21**, (2014).

[20] M. Greenwald et al., 20 years of research on the Alcator C-Mod tokamak, Phys Plasmas **21**, (2014).

[21] L. Gil et al., Stationary ELM-free H-mode in ASDEX Upgrade, Nuclear Fusion **60**, (2020).

[22] T. M. Wilks, A. M. Garofalo, P. H. Diamond, Z. B. Guo, J. W. Hughes, K. H. Burrell, and X. Chen, Scaling trends of the critical e × B shear for edge harmonic oscillation onset in DIII-D quiescent H-mode plasmas, Nuclear Fusion **58**, (2018).

[23] K. H. Burrell et al., *Advances in Understanding Quiescent H-Mode Plasmas in DIII-D*, in *Physics of Plasmas*, Vol. 12 (2005), pp. 1–10.

[24] W. Suttrop et al., Studies of the “Quiescent H-mode” regime in ASDEX Upgrade and JET, Nuclear Fusion **45**, 721 (2005).

[25] K. Miki and P. H. Diamond, Role of the geodesic acoustic mode shearing feedback loop in transport bifurcations and turbulence spreading, Phys Plasmas **17**, (2010).

[26] I. Cziegler, A. E. Hubbard, J. W. Hughes, J. L. Terry, and G. R. Tynan, Turbulence Nonlinearities Shed Light on Geometric Asymmetry in Tokamak Confinement Transitions, Phys Rev Lett **118**, (2017).

[27] E. S. Marmar, The alcator C-Mod program, Fusion Science and Technology **51**, 261 (2007).

[28] N. P. Basse et al., Diagnostic Systems on Alcator C-Mod, Fusion Science and Technology **51**, 476 (2007).

[29] A. Herrmann and O. Gruber, Chapter 1: ASDEX Upgrade-Introduction and Overview, Fusion Science and Technology **44**, 569 (2003).

[30] M. A. Chilenski, M. Greenwald, Y. Marzouk, N. T. Howard, A. E. White, J. E. Rice, and J. R. Walk, Improved profile fitting and quantification of uncertainty in experimental measurements of impurity transport coefficients using Gaussian process regression, Nuclear Fusion **55**, (2015).

[31] J. W. Hughes, D. Mossessia, K. Zhurovich, M. DeMaria, K. Jensen, and A. Hubbard, *Thomson Scattering Upgrades on Alcator C-Mod*, in *Review of Scientific Instruments*, Vol. 74 (2003), pp. 1667–1670.

[32] R. Fischer, C. J. Fuchs, B. Kurzan, W. Suttrop, and E. Wolfrum, Integrated data analysis of profile diagnostics at ASDEX upgrade, Fusion Science and Technology **58**, 675 (2010).

[33] B. Kurzan and H. D. Murmann, Edge and core Thomson scattering systems and their calibration on the ASDEX Upgrade tokamak, Review of Scientific Instruments **82**, (2011).

[34] S. K. Rathgeber, L. Barrera, T. Eich, R. Fischer, B. Nold, W. Suttrop, M. Willensdorfer, and E. Wolfrum, Estimation of edge electron temperature profiles via forward modelling of the electron cyclotron radiation transport at ASDEX Upgrade, Plasma Phys Control Fusion **55**, (2013).

[35] M. Willensdorfer, E. Wolfrum, R. Fischer, J. Schweinzer, M. Sertoli, B. Sieglin, G. Veres, and F. Aumayr, Improved chopping of a lithium beam for plasma edge diagnostic at ASDEX Upgrade, Review of Scientific Instruments **83**, (2012).

[36] A. Mlynek, G. Schramm, H. Eixenberger, G. Sips, K. McCormick, M. Zilker, K. Behler, and J. Eheberg, Design of a digital multiradian phase detector and its application in fusion plasma interferometry, Review of Scientific Instruments **81**, (2010).

[37] L. L. Lao, H. St JOHN, R. Stambaugh, A. Kellman, and W. Pfeiffer, Reconstruction of current profile parameters and plasma shapes in tokamaks, Nuclear Fusion **25**, (1985).

[38] P. J. McCarthy, P. Martin, and W. Schneider, The CLISTE Interpretive Equilibrium Code, 1999.

[39] R. S. Granetz, I. H. Hutchinson, J. Gerolamo, W. Pina, and C. Tsui, Magnetic diagnostics in Alcator C-MOD, Review of Scientific Instruments **61**, 2967 (1990).

[40] Y. Lin, J. Irby, P. Stek, I. Hutchinson, J. Snipes, R. Nazikian, and M. McCarthy, Upgrade of reflectometry profile and fluctuation measurements in Alcator C-Mod, Review of Scientific Instruments **70**, 1078 (1999).

[41] A. Q. Kuang, D. Brunner, B. Labombard, R. Leccacorvi, and R. Vieira, The flush-mounted rail Langmuir probe array designed for the Alcator C-Mod vertical target plate divertor, Review of Scientific Instruments **89**, (2018).

[42] L. Cupido, S. Graca, G. D. Conway, M. Manso, and F. Serra, *Frequency Hopping Millimeter-Wave Reflectometry in ASDEX Upgrade*, in *Review of Scientific Instruments*, Vol. 77 (2006).

[43] A. Lynn, Electron Cyclotron Emission Measurements of Coherent and Broadband Density Fluctuations in the Alcator C-Mod Tokamak Committee, The University of Texas at Austin, 2004.

[44] S. S. Denk et al., Analysis of electron cyclotron emission with extended electron cyclotron forward modeling, Plasma Phys Control Fusion **60**, (2018).

[45] S. S. Denk, R. Fischer, E. Poli, O. Maj, S. K. Nielsen, J. Rasmussen, M. Stejner, and M. Willensdorfer, ECRad: An electron cyclotron radiation transport solver for advanced data analysis in thermal and non-thermal fusion plasmas, Comput Phys Commun **253**, 107175 (2020).

[46] A. J. Creely, S. J. Freethy, W. M. Burke, G. D. Conway, R. Leccacorvi, W. C. Parkin, D. R. Terry, and A. E. White, Correlation electron cyclotron emission diagnostic and improved calculation of turbulent temperature fluctuation levels on ASDEX Upgrade, Review of Scientific Instruments **89**, (2018).

[47] V. I. Ilgisonis, V. P. Lakhin, A. I. Smolyakov, and E. A. Sorokina, Geodesic acoustic modes and zonal flows in rotating large-aspect-ratio tokamak plasmas, Plasma Phys Control Fusion **53**, (2011).

[48] K. Itoh, K. Hallatschek, and S. I. Itoh, Excitation of geodesic acoustic mode in toroidal plasmas, Plasma Phys Control Fusion **47**, 451 (2005).

[49] M. SASAKI, K. ITOH, A. EJIRI, and Y. TAKASE, Geodesic Acoustic Modes in Multi-Ion System, Plasma and Fusion Research **3**, S1017 (2008).

[50] N. Winsor, J. L. Johnson, and J. M. Dawson, Geodesic acoustic waves in hydromagnetic systems, Physics of Fluids **11**, 2448 (1968).

[51] M. SASAKI, K. ITOH, A. EJIRI, and Y. TAKASE, Modification of Symmetry of Poloidal Eigenmode of Geodesic Acoustic Modes, Plasma and Fusion Research **3**, 009 (2008).

[52] R. Hager and K. Hallatschek, Radial propagation of geodesic acoustic modes, Phys Plasmas **16**, (2009).

[53] G. D. Conway, C. Tröster, B. Scott, and K. Hallatschek, Frequency scaling and localization of geodesic acoustic modes in ASDEX Upgrade, Plasma Phys Control Fusion **50**, (2008).

[54] L. G. Eliseev, V. N. Zenin, S. E. Lysenko, and A. v. Melnikov, *Measurement of Geodesic Acoustic Modes and the Turbulent Particle Flux in the T-10 Tokamak Plasmas*, in *Journal of Physics: Conference Series*, Vol. 907 (Institute of Physics Publishing, 2017).

[55] C. A. de Meijere et al., Complete multi-field characterization of the geodesic acoustic mode in the TCV tokamak, Plasma Phys Control Fusion **56**, (2014).

[56] G. Wang et al., Multi-field characteristics and eigenmode spatial structure of geodesic acoustic modes in DIII-D L-mode plasmas, Phys Plasmas **20**, (2013).

[57] J. Cheng, L. W. Yan, K. J. Zhao, J. Q. Dong, W. Y. Hong, J. Qian, Q. W. Yang, X. T. Ding, X. R. Duan, and Y. Liu, Density fluctuation of geodesic acoustic mode on the HL-2A tokamak, Nuclear Fusion **49**, (2009).

[58] Y. Xu et al., Observation of geodesic acoustic modes (GAMs) and their radial propagation at the edge of the TEXTOR tokamak, Plasma Phys Control Fusion **53**, (2011).

[59] P. H. Diamond, S. I. Itoh, K. Itoh, and T. S. Hahm, *Zonal Flows in Plasma - A Review*, Plasma Physics and Controlled Fusion.

[60] G. D. Conway, A. I. Smolyakov, and T. Ido, Geodesic acoustic modes in magnetic confinement devices, Nuclear Fusion **62**, 013001 (2022).

[61] D. Zhou, Electromagnetic geodesic acoustic modes in tokamak plasmas, Phys Plasmas **14**, (2007).

[62] Z. Gao, L. Peng, P. Wang, J. Dong, and H. Sanuki, Plasma elongation effects on temperature gradient driven instabilities and geodesic acoustic modes, Nuclear Fusion **49**, (2009).

[63] E. Ayón-Beato, C. Campuzano, A. García, K. E. Weimer, E. A. Frieman, and J. L. Johnson, Geodesic Acoustic Mode in Toroidally Axisymmetric Plasmas with Non-Circular Cross Sections Localized Magnetohydrodynamic Instabilities in Tokamaks with Non-Circular Cross Sections, n.d.

[64] G. Merlo et al., Investigating the radial structure of axisymmetric fluctuations in the TCV tokamak with local and global gyrokinetic GENE simulations, Plasma Phys Control Fusion **60**, (2018).

[65] L. Villard et al., Global turbulence features across marginality and non-local pedestal-core interactions, Plasma Phys Control Fusion **61**, (2019).

[66] A. E. White et al., *Measurements of the Cross-Phase Angle between Density and Electron Temperature Fluctuations and Comparison with Gyrokinetic Simulations*, in *Physics of Plasmas*, Vol. 17 (2010).

[67] Z. Huang, S. Coda, G. Merlo, S. Brunner, L. Villard, B. Labit, and C. Theiler, Experimental observations of modes with geodesic acoustic character from the core to the edge in the TCV tokamak, Plasma Phys Control Fusion **60**, (2018).

[68] P. C. Stangeby, *The Plasma Boundary of Magnetic Fusion Devices* (Institute of Physics Pub, 2000).

[69] S. Wu and The EAST Team, An overview of the EAST project, Fusion Engineering and Design **82**, 463 (2007).

[70] C. Wahlberg, Geodesic acoustic mode induced by toroidal rotation in Tokamaks, Phys Rev Lett **101**, (2008).

[71] H. Ren and J. Cao, Landau damping of geodesic acoustic mode in toroidally rotating tokamaks, Phys Plasmas **22**, (2015).